This simple heuristic model describes the basic observed scale sizes of the dust emission in NGC 1068. But how does it relate to the true physical distribution of dust in active nuclei? The generic properties of dusty tori in AGNs have been discussed[3]. Because previously no observational means were available to resolve the dust distribution, early models for their dust emission[14–16] aimed mainly to reproduce the overall spectral energy distribution of Seyfert galaxies and quasars. These were calculated by two-dimensional radiative transfer through a smooth dust distribution. They can be divided in two classes: compact tori[14], where the dust fills a thick cylinder (with an axial hole) of a few parsecs in diameter, and extended fat disk models[15,16], with diameters of tens to hundreds of parsecs. Common to both classes was a very high absorption optical depth ($A_V > 100$, that is, $\tau_{12\mu} > 4$) in the equatorial plane. In preparation for our observations, we investigated the expected dust emission maps from those models by using three-dimensional radiative transfer[17]. They show that hot dust can only be observed from those surfaces that are both freely exposed to the radiation from the accretion disk and unobscured along the line of sight from the observer. In consequence, the observable structures at 8 and 12 μm are almost identical, and suffer very similar dust absorption. Obviously, this is not what we observe in NGC 1068.

The unification between Seyfert 1 and 2 galaxies[1] already seems to demand a geometrically thick dust distribution, the vertical height h (above the midplane) of which should be similar to its radius r, that is $h/r \approx 1$. By resolving the heated dust structure in NGC 1068 with MIDI/VLTI, we have demonstrated now that indeed $h/r \gtrsim 0.6$, even when allowing for projection effects. (Such effects seem to be small, because the axis of NGC 1068 as given by the outflow cone of ionized gas is inclined by only ~5° out of the plane of sky[18], thus excluding that an inclined thin disk could explain the apparent h/r).

Moreover, this thick structure is located at $r \leq 2$ pc. Thus, irradiation by the nuclear source will produce a hot inner wall—a 'funnel', which we identify as our hot component. As the average cloud temperatures are low, $T < 1{,}000$ K, it is not possible for gas pressure to support this structure vertically against gravity in the nuclear potential of NGC 1068.

In reality, it is very unlikely that gas and dust are distributed homogeneously in the torus: they will rather be confined to individual clouds[3]. A recent model for the overall spectral energy distributions[19] argues for a volume filling factor of <10%, and typically 5–10 clouds along an equatorial line of sight towards the centre. Much better resolution (<1 mas) would be required to distinguish such a torus from a homogeneous one. Turbulent motions of these clouds with average velocities $\langle v_T \rangle \approx 100\,\mathrm{km\,s^{-1}}$ (that is, similar to the random velocities that support the nuclear star cluster) could prevent the cloud system from collapsing. However, given these velocities and the large number of clouds along any line of sight, collisions between those clouds would be frequent, supersonic and highly inelastic. The turbulent motion would be damped within about one orbital period, t_{orb}(at $r = 2$ pc) $\approx 10^5$ yr. Thus, a continuous injection of kinetic energy into the cloud system seems to be required. To our knowledge, none of the current models of AGNs provide a convincing solution to this problem, although a very young nuclear star cluster might be able to provide the energy (but see ref. 3). This explanation requires AGN activity and nuclear starbursts to be intimately connected. So the present high-resolution observations of the nucleus of an active galaxy by infrared interferometry demand a better understanding of the physics of these spectacular objects. □

Received 3 February; accepted 1 April 2004; doi:10.1038/nature02531.

1. Antonucci, R. Unified models for active nuclei and quasars. *Annu. Rev. Astron. Astrophys.* **31,** 473–521 (1993).
2. Urry, C. M. & Padovani, P. Unified schemes for radio-loud active galactic nuclei. *Publ. Astron. Soc. Pacif.* **107,** 803–845 (1995).
3. Krolik, J. H. & Begelman, M. C. Molecular tori in Seyfert galaxies: Feeding the monster and hiding it. *Astrophys. J.* **329,** 702–711 (1998).
4. Antonucci, R. J. & Miller, J. S. Spectropolarimetry and the nature of NGC 1068. *Astrophys. J.* **297,** 621–632 (1985).
5. Lumsden, S. L. *et al.* Near- and mid-infrared imaging polarimetry of NGC 1068. *Mon. Not. R. Astron. Soc.* **303,** 209–220 (1999).
6. Leinert, C. *et al.* Ten-micron instrument MIDI: getting ready for observations on the VLTI. *Proc. SPIE* **4838,** 893–904 (2003).
7. Glindermann, A. *et al.* The VLTI—A Status Report. *Proc. SPIE* **4838,** 89–100 (2003).
8. Muxlow, T. W. B., Pedlar, A., Holloway, A. J., Gallimore, J. F. & Antonucci, R. R. J. The compact radio nucleus of the Seyfert galaxy NGC 1068. *Mon. Not. R. Astron. Soc.* **278,** 854–860 (1996).
9. Bock, J. J. *et al.* High spatial resolution imaging of NGC 1068 in the mid-infrared. *Astron. J.* **190,** 2904–2919 (2000).
10. Lutz, D. *et al.* ISO-SWS spectroscopy of NGC 1068. *Astrophys. J.* **536,** 697–709 (2000).
11. Kemper, F., Vriend, W. J. & Tielens, A. G. G. M. ISO spectra of Sgr A. *Astrophys. J.* (submitted).
12. Speck, A. K., Barlow, J. J., Sylvester, F. J. & Hofmeister, A. M. Dust features in the 10 micron infrared spectra of oxygen-rich evolved stars. *Astron. Astrophys. Suppl.* **146,** 437–464 (2000).
13. Maiolino, R. *et al.* Dust in active nuclei. I. Evidence for anomalous properties. *Astron. Astrophys.* **365,** 28–36 (2001).
14. Pier, E. A. & Krolik, J. H. Infrared spectra of obscuring dust tori around active galactic nuclei. *Astrophys. J.* **401,** 99–109 (1992).
15. Efstathiou, A., Hough, J. H. & Young, S. A model for the infrared continuum spectrum of NGC 1068. *Mon. Not. R. Astron. Soc.* **277,** 1134–1144 (1995).
16. Granato, G. L., Danese, L. & Franceschini, A. Thick tori around active galactic nuclei: the case for extended tori and consequences for their X-ray and infrared emission. *Astrophys. J.* **486,** 147–159 (1997).
17. Schartmann, M. *Dust Tori in Active Galactic Nuclei.* Thesis, Univ. Heidelberg (2003).
18. Crenshaw, D. M. & Kraemer, S. B. Resolved spectroscopy of the narrow-line region in NGC 1068: Kinematics of the ionized gas. *Astrophys. J.* **532,** L101–L104 (2000).
19. Nenkova, M., Ivezić, Z. & Elitzur, M. Dust emission from active galactic nuclei. *Astrophys. J.* **570,** L9–L12 (2002).
20. Bruhweiler, F. C., Miskey, C. L., Smith, A. M., Landsman, W. & Malumuth, E. Ionization, extinction and spiral structure in the inner disk of NGC 1068. *Astrophys. J.* **546,** 866–876 (2001).
21. Bland-Hawthorn, J. *et al.* The Ringberg standards for NGC 1068. *Astrophys. Space Sci.* **248,** 9–19 (1997).

Acknowledgements This Letter is based on observations carried out at the European Southern Observatory, Paranal, Chile, in the framework of the VLTI science demonstration program. MIDI could not have been built without contributions from many people, including E. J. Bakker, P. Ballester, S. Beckwith, P. Biereichel, A. Böhm, W. D. Cotton, S. Damstra, A. Glindemann, B. Grimm, J. de Jong, N. Haddad, H. Hanenburg, T. Henning, N. Housen, S. Hippler, W. Laun, S. Ligori, R. Lenzen, B. Lopez, O. von der Lühe, R. J. Mathar, J. Meisner, S. Morel, W. Morr, U. Neumann, R.-R. Rohloff, P. Schuller, N. Salm, C. Storz, A. Wallander and K. Wagner. We thank ESO staff at Garching, Santiago de Chile, and Cerro Paranal (Chile), for operating MIDI.

Competing interests statement The authors declare that they have no competing financial interests.

Correspondence and requests for materials should be addressed to W.J. (jaffe@strw.leidenuniv.nl).

Dislocation-driven surface dynamics on solids

S. Kodambaka, S. V. Khare, W. Święch, K. Ohmori, I. Petrov & J. E. Greene

Frederick Seitz Materials Research Laboratory and the Department of Materials Science, University of Illinois, 104 South Goodwin Avenue, Urbana, Illinois 61801, USA

Dislocations[1] are line defects that bound plastically deformed regions in crystalline solids. Dislocations terminating on the surface of materials can strongly influence nanostructural and interfacial stability, mechanical properties, chemical reactions, transport phenomena, and other surface processes. While most theoretical and experimental studies have focused on dislocation motion in bulk solids under applied stress[2,3] and step formation due to dislocations at surfaces during crystal growth[4–7], very little is known about the effects of dislocations on surface dynamics and morphological evolution. Here we investigate the near-equilibrium dynamics of surface-terminated dislocations using low-energy electron microscopy[8]. We observe, in real time, the thermally driven nucleation and shape-preserving growth of spiral steps rotating at constant temperature-dependent angular

velocities around cores of dislocations terminating on the (111) surface of TiN in the absence of applied external stress or net mass change. We attribute this phenomenon to point-defect migration from the bulk to the surface along dislocation lines. Our results demonstrate that dislocation-mediated surface roughening can occur even in the absence of deposition or evaporation, and provide fundamental insights into mechanisms controlling nanostructural stability.

Figure 1A and B illustrates the nucleation and growth of TiN(111) spiral steps and loops at the cores of dislocations terminating on TiN(111) surfaces, as observed *in situ* by low-energy electron microscopy (LEEM)[9] during annealing in N_2. (We define a loop as a two-dimensional (2D) island formed around a surface step segment pinned at both ends by dislocations.) Fig. 1A shows the formation of a concentric spiral step structure around a dislocation core, while the images in Fig. 1B capture the nucleation and growth of a closed loop. The spiral and loop steps both exhibit three-fold symmetry with a truncated-hexagonal shape, the near-equilibrium shape of 2D TiN(111) islands[10], indicative of fast step-edge diffusion. Note that these spirals and loops are observed during annealing with no net mass gain or loss and, as we will show, are quantitatively and qualitatively different from the growth structures predicted by Burton, Cabrera and Frank[7] ('BCF'), and step curvature-driven surface dynamics[11].

A remarkable feature is revealed in Fig. 1A, a–d: the spiral steps rotate around the dislocation core, resulting in an increase in the total step length with time t as the spirals undergo a shape-preserving anticlockwise motion with a constant angular velocity ω. That is, the shape and size of the spiral are periodic with time $\tau = 2\pi/\omega$. For the spiral shown in Fig. 1A, a–d, $\tau = 47$ s corresponds to one complete rotation at the annealing temperature $T = 1{,}688$ K; the spiral shown in Fig. 1A, a, is geometrically identical to the one in Fig. 1A, d. During the period τ, the layer labelled 3 disappears from the field of view in Fig. 1A, c, and a new layer, labelled 0, is formed (Fig. 1A, d) as the dislocation core climbs by a unit step height, $a_\perp = 2.4$ Å, normal to the surface.

Nucleation and growth of a loop originating at a defect is shown in Fig. 1B, a–c. Upon detaching from the defect, the expanding loop (Fig. 1B, d) regains the equilibrium shape of 2D TiN(111) islands[10]. This process, like the nucleation and growth of spiral steps, is also periodic. For the loops shown in Fig. 1B, a–d, $\tau = 85 \pm 5$ s corresponds to the loop nucleation period at $T = 1{,}653$ K.

Analogous to the growth spirals and loops observed in bulk solids owing to the operation of Frank–Read[12] and/or Bardeen–Herring[13] sources under applied stress[14], and on surfaces during crystal growth as predicted by the BCF theory[7], the features observed in Fig. 1A and B are due to surface steps pinned by a single dislocation (in the case of a spiral) and a pair of oppositely signed dislocations (for a loop), respectively. For a single dislocation, the steps emanating from the cores wind into expanding spirals. With a pair of oppositely signed dislocations, as illustrated in the schematic diagram of Fig. 1C, the expanding spirals originating from the cores rotate in opposing directions, eventually coming into contact to form a loop that increases in size.

Figure 2a is a representative plot of the areas A of a TiN(111) spiral and an adjacent surface loop (both are shown in the corresponding LEEM image, right) as a function of time t at 1,653 K. The two sets of data correspond to successive spirals and loops originating periodically from their respective sources. We observe that at constant temperature, spirals and loops have the same generation times ($\tau = 85 \pm 5$ s for the examples shown in the LEEM image in Fig. 2a, $T = 1{,}653$ K) and that their areas increase linearly with time. The similarity in dA/dt and ω for the two types of structures suggests that the same mechanism controls their growth. The observed step growth is a localized process that occurs only at the dislocation cores. This is in contrast to the BCF model, where the

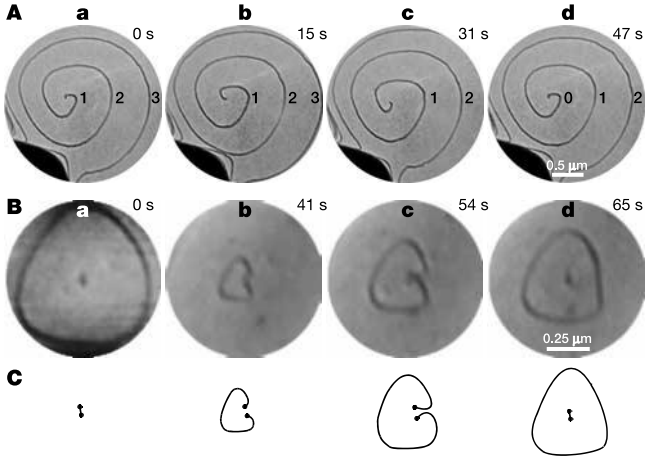

Figure 1 Nucleation and growth of spiral steps on TiN(111). Low-energy electron microscopy (LEEM) images showing nucleation and growth of bilayer-height surface steps at the cores of dislocations terminating on TiN(111) terraces during annealing in N_2 at temperatures T. The images were acquired as a function of time t. The dark lines in the LEEM images are ⟨110⟩-oriented bilayer-height steps (the [111] direction in B1-NaCl structure TiN is polar, consisting of alternating layers of Ti and N atoms). **A**, Field of view ~2.53 μm; $T = 1{,}688$ K. Spiral steps form owing to the pinning of a step edge at a dislocation core. **B**, Field of view ~0.93 μm; $T = 1{,}653$ K. Loops nucleate and grow centred around a step edge pinned at both ends by dislocations of opposite sign. **C**, Schematic diagram of the loop generation process observed in **B**.

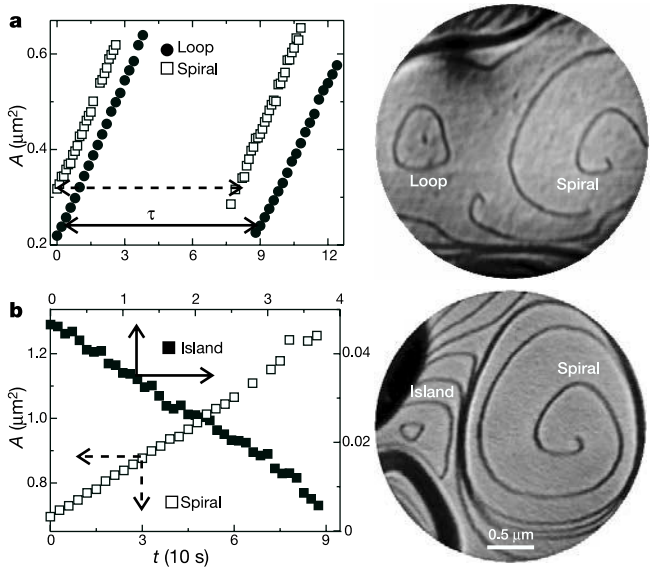

Figure 2 Area versus annealing time for 2D TiN loops, spirals and islands on TiN(111). **a**, Time-dependent areas A of 2D TiN loops and spirals on a TiN(111) surface (shown in the image to the right) during annealing at $T = 1{,}653$ K. (We only measure areas of loops that formed upon detaching from the central core and have attained near-equilibrium truncated-hexagonal shapes as in Fig. 1B, d.) Spiral areas are calculated as $A(t) = \frac{1}{2}\int_{\theta_1}^{\theta_2}[r(\theta,t)]^2 d\theta$. The spiral shape function $r(\theta,t)$ is defined for θ in the range 0 to ∞, and $\theta_1 \le \theta \le \theta_2$ corresponds to an outwardly moving spiral step segment far from the core. Because loop areas increase linearly with time, while the growth rates of spirals with high curvatures ($>2 \times 10^{-4}$ Å^{-1}) near the core are nonlinear, we only measure areas of spirals corresponding to linear growth rates with $\theta_1 = \pi$ and $\theta_2 = 3\pi$. τ is the average time required to generate successive spirals and loops that have the same area. **b**, The time-dependent areas A of spirals and 2D TiN islands on TiN(111) terraces (shown in the image to the right) during annealing at $T = 1{,}694$ K. Note that the left and bottom axes of the plot correspond to that of the spiral, while the right and top axes correspond to the island. The spiral area increases linearly with time while the island area decreases. The fields of view in both images are ~2.75 μm.

growth flux is non-localized, resulting in a curvature-dependent step velocity of spirals and loops whose areas increase nonlinearly with time[7].

Figure 2b contains A versus t plots for a 2D TiN(111) adatom island and an adjacent spiral (shown in the associated LEEM image, right) during annealing at 1,694 K. Note that the island area decreases linearly with t while the spiral area increases. Previous studies[15] have shown that step-edge attachment/detachment is the rate-limiting mechanism for the curvature-driven decay of 2D TiN adatom and vacancy islands on TiN(111) terraces. The above results, typical of data from over 50 adatom islands and 9 spirals acquired at temperatures 1,500–1,700 K, demonstrate that the mechanism of surface spiral and loop growth is quite distinct from that of 2D TiN(111) island decay (Ostwald ripening)[11]. We suggest, and provide experimental evidence below, that the observed nucleation and growth of spiral steps during annealing is due to dislocation-assisted bulk diffusion.

Our model for this phenomenon is based upon two assumptions. (1) A non-equilibrium concentration of point defects exists in the bulk. This is reasonable based upon the fact that TiN is known to have a very wide single-phase region and can sustain both high anion (N) and cation (Ti) vacancy concentrations[16]. Given that we observe steps emanating from the grooves (the thick dark lines visible in the LEEM images in Figs 1, 2 and 3) annihilating the spiral steps, we conclude that spirals grow inward, normal to the surface.

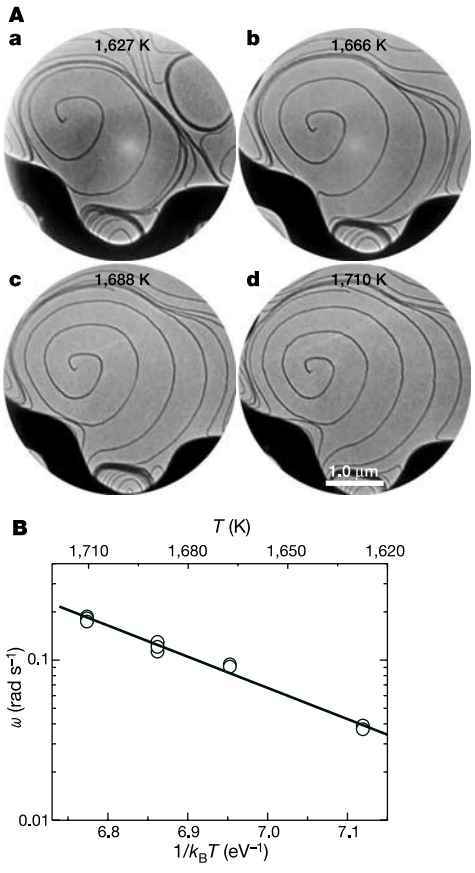

Figure 3 Temperature dependence of angular velocities of spirals on TiN(111). **A**, LEEM images (fields of view ~3.79 μm) of TiN spiral steps on a TiN(111) terrace. The images were acquired as a function of temperature T. **B**, Angular velocity ω of the spirals, plotted as a function of $1/T$. ω is determined by fitting a function of the form $r(\theta,t) = a(\theta)[\theta + \omega t]$, where $a(\theta)$ is a time-independent shape function, to the time-dependent spiral step boundary coordinates obtained from the LEEM images. The solid line is fitted to the $\omega(T)$ data with a function of the form $\omega(T) = \omega_o \exp(-E_d/kT)$ using least-squares analyses. We obtain $\omega_o = 10^{12\pm0.5}\,s^{-1}$ with $E_d = 4.5 \pm 0.2$ eV.

Note, however, that there is no net mass gain or loss. The surface point-defect concentration C_s^{eq}, however, is at thermal equilibrium, because a N-terminated surface is energetically favourable for TiN(111) (ref. 17). (2) Dislocation cores emit/absorb point defects at a thermally activated time-independent rate R; a plausible assumption given that dislocation cores act as sources/sinks for point defects[18,19].

Consider for simplicity a circular loop of radius r_{loop} centred around a core region of finite radius r_{core}. The surface point-defect concentration $C(r)$ at any position r, with $r_{core} < r < r_{loop}$, is given by the diffusion equation $\partial C(r)/\partial t = D_s \nabla^2 C(r)$, where D_s is the surface diffusivity. Within the quasistatic approximation in which surface diffusion of adatoms is much faster than the step-edge velocity, $\partial C(r)/\partial t = 0$. The general solution of the resulting Laplace equation $\nabla^2 C(r) = 0$ is $C(r) = C_1 \ln(r) + C_2$, where the constants C_1 and C_2 are determined by the boundary conditions at the core and the loop. From assumption (2) above, the flux $-D_s \nabla C(r)$ of point defects at the core is

$$-D_s \nabla C(r)|_{r=r_{core}} = \frac{R}{2\pi r_{core}} \tag{1a}$$

while at the loop:

$$-D_s \nabla C(r)|_{r=r_{loop}} = k_s[C(r_{loop}) - C_{loop}^{eq}] \tag{1b}$$

In equation (1b), k_s is the rate of attachment/detachment at the step and $C_{loop}^{eq} = C_s^{eq} \exp(\mu_{loop}/k_B T)$, from the Gibbs–Thomson relation[11], is the equilibrium point-defect concentration due to the curvature-dependent chemical potential μ_{loop} associated with the loop. Solving for C_1 and C_2 yields the normal component of the loop velocity dr_{loop}/dt as

$$\frac{dr_{loop}}{dt} = \Omega k_s \left[C(r_{loop}) - C_{loop}^{eq}\right] = \frac{\Omega}{2\pi r_{loop}} R \tag{2}$$

where Ω is the unit TiN molecular area. In deriving the above formalism, we have neglected the curvature-driven flux from the loop to the local environment. In the detachment-limited regime, the contribution to dr_{loop}/dt due to this flux, which is proportional to $-1/r_{loop}$, is small and hence will have little effect on the growth velocity dr_{loop}/dt in equation (2). The important point is that the form of equation (2) is qualitatively different from the parallel equation describing the 2D island decay (Ostwald ripening) process[15]. We note that equation (2) is also valid, without loss of generality, for non-circular loops and spiral steps far from the core. Clearly, from equation (2), the loop (and spiral) growth rate $dA/dt = \Omega R$ is time-invariant, consistent with the constant slopes obtained in our measurements of A versus t in Fig. 2.

For the steady-state growth of a spiral rotating around a dislocation core, we obtain from mass conservation the relation $\omega = 2\pi \Omega R/A_o$, indicating that the frequency ω is thermally activated. A_o in the above relation is the area encompassing the spiral structure over which R is non-negligible. Substituting the experimental data for dA/dt and ω into our model, we obtain A_o values between 0.25 and 0.32 μm^2, which are less than the areas encompassed by spiral boundaries. Our measurements of $(dA/dt)/\omega$ (which is proportional to A_o) versus T suggest that A_o is independent of temperature. However, understanding the physical significance of A_o requires further investigation.

Typical ω values, determined from separate sets of LEEM images acquired at four different temperatures T (see Fig. 3A) are plotted as a function of $1/T$ in Fig. 3B. From the $\omega(T)$ data, we find an activation energy $E_d = 4.5 \pm 0.2$ eV, with a prefactor of $10^{12\pm0.5}\,s^{-1}$, compared to 2.3 ± 0.6 eV for the decay of 2D TiN islands on TiN(111) (ref. 15). A constant ω for a given T implies that the dislocation climb velocity normal to the surface is also time-invariant. Hence, E_d corresponds to the activation barrier for dislocation motion, which is generally associated with point-defect formation and migration along the dislocation (also referred to as

pipe "diffusion")[20]. The fact that we measure a higher activation barrier E_d for spiral growth than for island decay (and E_d is significantly lower than the desorption energies for TiN and Ti adspecies[17]) provides strong evidence that the dominant mass transport is along dislocation lines rather than surface diffusion or evaporation. This is physically reasonable because bulk point-defect migration, expected to influence surface dynamics at sufficiently high temperatures[21], has a smaller activation barrier along dislocation lines[20] than in dislocation-free areas.

In formulating equation (2), we assume an equilibrium defect concentration C_{loop}^{eq} associated with the loop. This is justified for the first loop, as steps near the core and far from the boundary maintain a truncated-hexagonal shape with three-fold symmetry, the equilibrium shape of TiN(111) steps. (This observation also suggests that localized growth flux at the cores may have negligible effect on step shapes.) However, far from the cores we find, first, steps with non-equilibrium shapes that vary with the spiral geometry and, second, step bunching. We attribute these observations to the presence of grooves bounding the spirals. Hence, modelling growth kinetics of multiple loop/spiral steps requires a better understanding of the effects of the geometric constraints imposed by physical boundaries on step chemical potentials.

Finally, our model assumes a constant rate R, which depends on two driving forces: first, equilibration of bulk point-defects, and second, minimization of dislocation line energy. In the first case, R is a function of the concentration gradient between the surface and the bulk, which decreases with time (K. McCarty and N. C. Bartelt, personal communication). Hence, this driving force terminates upon equilibration of the bulk point-defect concentration. In the second case, however, spiral and loop growth will continue to occur until the disappearance of the dislocation core. Our preliminary A versus t data for loops and spirals indicate that dA/dt systematically decreases by $\leq$4% for successive generation of new spirals and loops. This, however, is within experimental uncertainties of $\sim$10%. Thus, additional experiments for extended annealing times are necessary to quantitatively determine the time-dependence, if any, in dA/dt and hence the dominant driving force.

We expect the near-equilibrium spiral step growth process described above to be general, and that it will be observed for other materials. In contrast to recent work showing surface[15,22] and bulk[21] transport dominated 2D island dynamics, the present study demonstrates that facile bulk diffusion along the dislocations can lead to both qualitatively and quantitatively different surface evolution kinetics. □

Received 10 October 2003; accepted 11 March 2004; doi:10.1038/nature02495.

1. Cottrell, A. H. in *Dislocations and Plastic Flow in Crystals* (eds Fowler, R. H., Kapitza, P., Mott, N. F. & Bullard, E. C.) Ch. 1 (Oxford Univ. Press, London, 1953).
2. Bulatov, V., Abraham, F. F., Kubin, L., Devincre, B. & Yip, S. Connecting atomistic and mesoscale simulations of crystal plasticity. *Nature* **391,** 669–672 (1998).
3. Lagow, B. W. *et al.* Observation of dislocation dynamics in the electron microscope. *Mater. Sci. Eng. A* **309–310,** 445–450 (2001).
4. Verma, A. R. & Amelinckx, S. Spiral growth on carborundum crystal faces. *Nature* **167,** 939–940 (1951).
5. Teng, H. H., Dove, P. M., Orme, C. A. & De Yoreo, J. J. Thermodynamics of calcite growth: Baseline for understanding biomineral formation. *Science* **282,** 724–727 (1998).
6. Pina, C. M., Becker, U., Risthaus, P., Bosbach, D. & Putnis, A. Molecular-scale mechanisms of crystal growth in barite. *Nature* **395,** 483–486 (1998).
7. Burton, W. K., Cabrera, N. & Frank, F. C. The growth of crystals and the equilibrium structure of their surfaces. *Phil. Trans. R. Soc. Lond. A* **243,** 299–358 (1951).
8. Bauer, E. Low-energy electron microscopy. *Rep. Prog. Phys.* **57,** 895–938 (1994).
9. Tromp, R. M. & Reuter, M. C. Design of a new photo-emission/low-energy electron microscope for surface studies. *Ultramicroscopy* **36,** 99–106 (1991).
10. Kodambaka, S. *et al.* Absolute TiN(111) step energies from analysis of anisotropic island shape fluctuations. *Phys. Rev. Lett.* **88,** 146101 (2002).
11. Zinke-Allmang, M., Feldman, L. C. & Grabow, M. H. Clustering on surfaces. *Surf. Sci. Rep.* **16,** 377–463 (1992).
12. Frank, F. C. & Read, W. T. Multiplication processes for slow moving dislocations. *Phys. Rev.* **79,** 722–723 (1950).
13. Bardeen, J. & Herring, C. in *Imperfections in Nearly Perfect Crystals* (eds Shockley, W., Hollomon, J. H., Maurer, R. & Seitz, F.) Chap. 10 (Wiley, New York, 1952).
14. Hull, D. & Bacon, D. J. *Introduction to Dislocations* Ch. 8 (Pergamon, Oxford, 1984).
15. Kodambaka, S. *et al.* Size-dependent detachment-limited decay kinetics of two-dimensional TiN islands on TiN(111). *Phys. Rev. Lett.* **89,** 176102 (2002).
16. Sundgren, J. E., Johansson, B. O., Rockett, A., Barnett, S. A. & Greene, J. E. in *Physics and Chemistry of Protective Coatings* (eds Greene, J. E., Sproul, W. D. & Thornton, J. A.) 95–115 (American Institute of Physics, New York, 1986).
17. Gall, D., Kodambaka, S., Wall, M. A., Petrov, I. & Greene, J. E. Pathways of atomistic processes on TiN(001) and (111) surfaces during film growth: an *ab initio* study. *J. Appl. Phys.* **93,** 9086–9094 (2003).
18. Weertman, J. & Weertman, J. R. in *Elementary Dislocation Theory* (eds M. E., Weertman, J. & Weertman, J. R.) Ch. 6 (Macmillan, New York, 1964).
19. Justo, J. F., de Koning, M., Cai, W. & Bulatov, V. V. Point defect interaction with dislocations in silicon. *Mater. Sci. Eng. A* **309–310,** 129–132 (2001).
20. Indenbom, V. L. & Saralidze, Z. K. in *Elastic Strain Fields and Dislocation Mobility* (eds Indenbom, V. L. & Lothe, J.) Ch. 10 (Elsevier Science, Amsterdam, 1992).
21. McCarty, K. F., Nobel, J. A. & Bartelt, N. C. Vacancies in solids and the stability of surface morphology. *Nature* **412,** 622–625 (2001).
22. Giesen, M. Step and island dynamics at solid/vacuum and solid/liquid interfaces. *Prog. Surf. Sci.* **68,** 1–153 (2001).

Acknowledgements This work was supported by the US Department of Energy (DOE), Division of Materials Science, through the University of Illinois Frederick Seitz Materials Research Laboratory (FS-MRL). We thank C. P. Flynn, H. Birnbaum, R. J. Pflueger and P. O. Å. Persson for discussions and critical reading of the manuscript. We also appreciate the use of the facilities in the Center for Microanalysis of Materials, partially supported by DOE, at the FS-MRL.

Competing interests statement The authors declare that they have no competing financial interests.

Correspondence and requests for materials should be addressed to S.K. (kodambak@uiuc.edu).

Polymerization within a molecular-scale stereoregular template

Takeshi Serizawa*, Ken-ichi Hamada & Mitsuru Akashi*

Department of Nanostructured and Advanced Materials, Graduate School of Science and Engineering, Kagoshima University, 1-21-40 Korimoto, Kagoshima 890-0065, Japan

* Present addresses: Research Center for Advanced Science and Technology, The University of Tokyo, 4-6-1 Komaba, Meguro-ku, Tokyo 153-8904, Japan (T.S.); Department of Molecular Chemistry, Graduate School of Engineering, Osaka University, 2-1 Yamada-oka, Suita 565-0871, Japan (M.A.)

Enzymes efficiently synthesize biopolymers by organizing monomer units within regularly structured molecular-scale spaces and exploiting weak non-covalent interactions, such as hydrogen bonds, to control the polymerization[1] process. This 'template' approach is both attractive and challenging for synthetic polymer synthesis, where structurally regulated molecular-scale spaces could in principle provide solid-phase reaction sites for precision polymerization. Previously, free-radical polymerization of methyl methacrylate in solutions containing stereoregular isotactic (it) or syndiotactic (st) poly(methyl methacrylate) (PMMA) has been shown to result in template synthesis[2,3] of the opposite PMMA based on stereocomplex formation[4,5] with van der Waals interactions. However, using the structure of a solid to determine the stereochemical structure of a polymer has not been satisfactorily achieved[6]. Here we show that macromolecularly porous ultrathin films, fabricated by a single assembly step, can be used for the highly efficient stereoregular template polymerization of methacrylates through stereocomplex formation. This reaction mould accurately transfers its structural properties of stereoregularity, molecular weight and organization within the template to the new polymer.

Structurally regulated molecular-scale spaces (nanospaces) in ultrathin polymer films are potentially valuable as solid-phase reaction sites for precision polymerization. As the macromolecular mobility is restricted in the solid state, the template effect of a constituent polymer is potentially accelerated. It is, however, difficult